Journal of Colloid and Interface Science 677 (2025) 352–364

Contents lists available at ScienceDirect

Journal of Colloid And Interface Science

journal homepage: www.elsevier.com/locate/jcis

Kinetic monitoring of molecular interactions during surfactant-driven self-propelled droplet motion by high spatial resolution waveguide sensing

Eniko Farkas [a], Kinga Dóra Kovács [a,b], Inna Szekacs [a], Beatrix Peter [a], István Lagzi [c,d], Hiroyuki Kitahata [e], Nobuhiko J. Suematsu [f,g,*], Robert Horvath [a,h,*]

[a] Nanobiosensorics Laboratory, Institute of Technical Physics and Materials Science, HUN-REN Centre for Energy Research, 1121 Budapest, Hungary
[b] Department of Biological Physics, Eötvös Loránd University, 1117 Budapest, Hungary
[c] Department of Physics, Institute of Physics, Budapest University of Technology and Economics, Muegyetem rkp. 3, 1111 Budapest, Hungary
[d] HUN-REN–BME Condensed Matter Physics Research Group, Budapest University of Technology and Economics, Muegyetem rkp. 3, 1111 Budapest, Hungary
[e] Graduate School of Science, Chiba University, Yayoi-cho 1-33, Inage-ku, Chiba 263-8522, Japan
[f] Meiji Institute of Advanced Study of Mathematical Sciences (MIMS), Meiji University, 4-21-1 Nakano, Tokyo 164-8525, Japan
[g] Graduate School of Advanced Mathematical Sciences, Meiji University, 4-21-1 Nakano, Tokyo 164-8525, Japan
[h] Nanobiosensorics Laboratory, Institute of Biophysics, HUN-REN Biological Research Centre, Szeged, Hungary

GRAPHICAL ABSTRACT

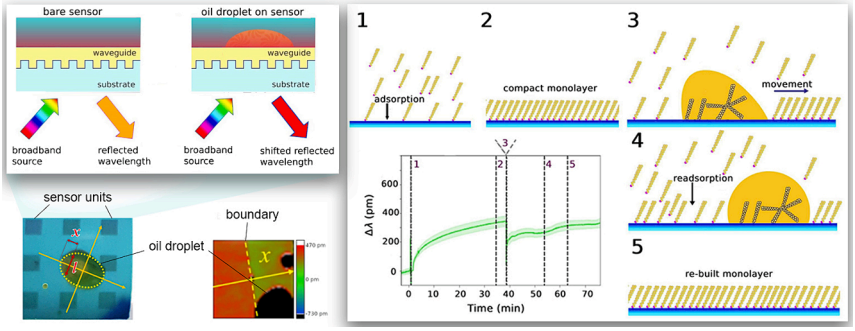

ARTICLE INFO

Keywords:
Resonant waveguide grating imager
OWLS optical biosensor
Droplet motion
Self-propelled motion
Self-assembly
Oil/water interfaces
Marangoni effect
Characterization of surface properties

ABSTRACT

Hypothesis: Self-driven actions, like motion, are fundamental characteristics of life. Today, intense research focuses on the kinetics of droplet motion. Quantifying macroscopic motion and exploring the underlying mechanisms are crucial in self-structuring and self-healing materials, advancements in soft robotics, innovations in self-cleaning environmental processes, and progress within the pharmaceutical industry. Usually, the driving forces inducing macroscopic motion act at the molecular scale, making their real-time and high-resolution investigation challenging. Label-free surface sensitive measurements with high lateral resolution could *in situ* measure both molecular-scale interactions and microscopic motion.

Experiments: We employ surface-sensitive label-free sensors to investigate the kinetic changes in a self-assembled monolayer of the trimethyl(octadecyl)azanium chloride surfactant on a substrate surface during the

* Corresponding authors at: Meiji Institute of Advanced Study of Mathematical Sciences (MIMS), Meiji University, 4-21-1 Nakano, Tokyo 164-8525, Japan (N.J. Suematsu); Nanobiosensorics Laboratory, Institute of Technical Physics and Materials Science, HUN-REN Centre for Energy Research, 1121 Budapest, Hungary (R. Horvath).
E-mail addresses: suematsu@meiji.ac.jp (N.J. Suematsu), horvath.robert@ek.hun-ren.hu (R. Horvath).

https://doi.org/10.1016/j.jcis.2024.07.236
Received 30 January 2024; Received in revised form 29 July 2024; Accepted 30 July 2024
Available online 8 August 2024

Droplet-surfactant interaction
Adsorption

self-propelled motion of nitrobenzene droplets. The adsorption–desorption of the surfactant at various concentrations, its removal due to the moving organic droplet, and rebuilding mechanisms at droplet-visited areas are all investigated with excellent time, spatial, and surface mass density resolution.

Findings: We discovered concentration dependent velocity fluctuations, estimated the adsorbed amount of surfactant molecules, and revealed multilayer coverage at high concentrations. The desorption rate of surfactant ($18.4\ s^{-1}$) during the microscopic motion of oil droplets was determined by *in situ* differentiating between droplet visited and non-visited areas.

1. Introduction

Motion is one of the essential behaviors of living organisms. In the past several decades, considerable efforts have been devoted to designing and investigating self-propelled motion in inanimate systems to mimic the motion of organisms [1–3]. In these systems, the moving entities are vesicles [4], solid particles [5], and droplets of various sizes propelled at the liquid–air and liquid–solid interfaces [6–8], and in the bulk liquid phase [9–11]. The related mechanism of the motion can be diversified. In several cases, the motion is generated by a nonuniform distribution of surfactant around the object, which is translated into the net force acting on the droplet [12–19]. In other cases, this phenomenon can generate fluid flow inside the droplets/vesicles, contributing to the development of Marangoni flow inside them, which governs the motion [20–25].

The motion of the droplet determines the formation of a monomolecular layer due to the suspension gradient. No layer will form if this movement is too slow or fast. Such molecular-scale processes are also crucial for the development of self-structuring [26,27] and self-healing materials [28], as well as for the pharmaceutical industry [29–31] development or printing industry [32,33]. Macroscopic and nanoscale movements also influence biological processes, where a conformational change can be induced, governing subsequent motion [34]. These phenomena are based on the fundamental principle of molecular-scale self-assembly, where higher-order processes trigger self-assembling movements. This occurs on solid–liquid film interfaces or other surfaces. At the end of the process, the self-propelled droplet can remove contaminant molecules via adsorption, thus contributing to self-cleaning or bioremediation technologies [31,35–39]. One of the categories of these motions occurs at either the liquid–solid or gas–solid interface [13,15,40–44]. In all cases, the motion of the liquid droplets at the solid substrate results from the imbalance in the forces due to the surface tension acting on the liquid–solid contact line. Until now, the investigations of active droplet motion on a solid interface have predominantly focused on the dynamic aspects of the cause of the motion. They are, namely, the characterization and description of the forces generated and, based on this knowledge, how the motion can be controlled and directed. However, no attention has been devoted to investigating the (spatio)temporal change in the characteristics of the solid surface and the self-assembled films, which is a crucial factor in designing and engineering new self-propelled systems. This is predominantly, due to the lack of appropriate techniques capable of monitoring changes in nanometer-scale thin layers, and the macroscopic motion of the droplet simultaneously. Therefore, the dynamic changes in the self-assembled films were simply overlooked.

This study investigates a system in which the surfactants dissolved in the water are adsorbed to the solid surface, and then an organic droplet is placed on the surface. The interfacial tension around the droplet is homogeneous at the beginning of the experiments. Then, surfactant molecules on the solid surface are desorbed and dissolved in the organic droplet. Due to the small perturbation, the contact angle and the corresponding surface tension vary around the droplet, creating a net force generating the motion of the droplet [13]. To understand more deeply the underlying mechanism and dynamics of the motion, an important aspect is to gain information about the timescale of the formation of self-assembled monolayer of surfactants in the solid–liquid interface, quantify the desorbed amount of the surfactant molecules caused by the droplet and reveal the kinetics of the rebuilding of the monolayer. To achieve them, we used surface-sensitive label-free optical methods, namely the resonant waveguide grating (RWG) with improved lateral resolution [45] and optical waveguide lightmode spectroscopy (OWLS) [46,47], and quartz crystal microbalance (QCM) [48–50], both equipped with a flow-through liquid cell.

Evanescent field-based surface-sensitive label-free optical techniques, such as surface plasmon resonance (SPR) [51–53], OWLS, and RWG, have emerged as powerful tools for characterizing the self-assembly of (bio)molecular layers on solid surfaces with sub-nanometer resolution in the thickness of the assembled films. These techniques allow for real-time monitoring of molecular adsorption, desorption, and self-organization on solid surfaces, with high sensitivity and specificity. The operating principle of the above-mentioned label-free optical techniques is based on measuring changes in the refractive index (RI) in the close vicinity of the sensor surface. These sensing methods apply evanescent electromagnetic fields generated by coupling a free space propagating laser light into a bound optical mode of the transducer. This is typically achieved using a high refractive index prism or coupling gratings [50]. The evanescent field component of the excited bound optical mode is localized at the sensor surface and diminishes with an exponentially decaying intensity in the bulk liquid media introduced above the sensor. These methods offer a significant advantage by providing high sensitivity by examining a relatively large surface area close to the sensor surface, typically within a thickness range of 0–200 nm. In general, the detected response signal is directly proportional to the overall shift in the effective RI of the employed surface-bound optical mode. The effective refractive index shift depends on the change in the local refractive index within the evanescent field [50].

SPR is based on the excitation of surface plasmons at a metal-dielectric interface, and the change in the monitored RI is usually detected as a shift in the resonance angle needed to excite the surface plasmon mode by a light beam introduced to the interface through a prism. Conventional SPR sensors are limited in performing structural analysis of the surface deposited layers because they can only employ a single optical mode with transverse magnetic (TM) polarization. As a result, by measuring a single quantity only, namely the change in the effective refractive index of this mode, it is not possible to determine the two independent refractive index (n_A) and thickness (d_A) parameters of the surface adsorbed molecular films. Instead, the SPR signal is calibrated using an approximate relationship (typically one resonant unit (RU) $\approx$ 1 ng cm^{-2}) to determine the surface mass density (M) of the investigated analyte [50].

OWLS and RWG are based on the excitation of surface-bound optical modes (guided or waveguide modes) in a high refractive index thin-film planar optical waveguide. The change in the effective refractive index is usually monitored by following the shifts in the resonant angle needed for waveguide mode coupling or the shifts in the reflected light intensity or wavelength at maximal mode excitation. The sensitivity and high-throughput capability (96 or 384 well microplate-based formats) of RWG sensors allow for the examination of a wide range of biological, chemical, and biophysical processes, and phenomena in a completely label-free manner, providing valuable insights into various systems and their kinetic processes [45,54–57]. Similar to SPR, it can employ only one type of polarized mode, the 0th-order optical waveguide mode with

TM polarization. In contrast, the OWLS sensor can quantify the layer build-up and structure of the adsorbed molecular layers with greater detail but uses a single sensor only. OWLS was demonstrated to follow the self-assembly of organic molecules or the formation of polyelectrolyte catalyst layers [58–60]. Of note, self-assembled layers were investigated by SPR, too [61–63]. In contrast to SPR, the OWLS device employs two surface modes with orthogonal polarizations, namely the 0th-order waveguide mode with transverse electric (TE) and TM polarization. By detecting these two independent modes, the optogeometrical parameters of the surface adsorbed layers and their structure can be characterized, and both the thickness and refractive index of the adsorbed layers (n_A, d_A) can be determined together with the M of the assembled films [50]. The OWLS sensor is also well-suited for the detailed analysis of molecular scale ordering [64], such as revealing the surface orientation of bioreceptors in label-free bioassays [50,65–67].

Until now, the RWG biosensors have found their primary application in cellular assays, monitoring the real-time process of cellular adhesion and the role of the glycocalyx in adhesion [47]. RWG can also be used to study the behavior of living cells under flow conditions in real-time [55]. Significantly, the application of RWG biosensors extends beyond studying cell populations; they can also be utilized for investigating individual cells due to the high spatial resolution available in state-of-the-art systems. Notably, Ferrie *et al.* have developed an RWG sensor (high-frequency RWG imager) capable of performing wavelength shift and intensity modulation-based measurements to monitor detailed beating patterns of cardiomyocyte cells [68]. Due to its high resolution (RWG biosensors a spatial resolution of 25 μm and a sampling time of 3 s), RWG sensors can analyze the adhesion kinetics of cancer cells [69] and cancer cell invasion into a 3D Matrigel film [70]. In another work, the RWG biosensor with single-cell resolution was combined with robotic fluidic force microscopy (Robotic FluidFM), achieving an unprecedented throughput in the single-cell adhesion force measurements of large cell populations. When the surface adsorption of biomolecules is investigated, RWG can monitor the surface adsorbed mass density in real-time after a simple calibration procedure [47].

In the present work, we applied these powerful optical waveguide methods in a completely different scientific field for the in-situ monitoring of the motion of organic droplets and the underlying driving processes with molecular-scale resolution. We utilized the RWG, QCM, and OWLS sensors with flow through cuvette arrangements to investigate the kinetics of self-assembled monolayer formation of the trimethyl (octadecyl)azanium chloride, also called as stearyltrimethylammonium chloride (STAC) surfactant, playing a vital role during the self-propelled motion of organic droplets. The adsorption–desorption of the STAC surfactant on the sensor surfaces and the orientation of the adsorbed molecules were all monitored. Uniquely, both the droplet motion and the kinetic changes in the STAC layer were investigated *in situ* using a high spatial resolution RWG device. The regeneration kinetics of the self-assembled monolayer at surface areas visited by the moving droplet were also revealed and studied for the first time. By combining the capabilities of QCM, RWG, and OWLS, we achieve a more comprehensive understanding of the droplet-surfactant interaction, including the kinetic mechanisms of self-propelled droplet motion at the molecular scale and the characterization of the surface mass density and structure of the surfactant films.

2. Materials and methods

2.1. OWLS instrument and related protocols for monitoring the surface assembly of STAC layers from bulk solutions

An OWLS210 instrument (MicroVacuum Ltd., Budapest, Hungary) was used to *in situ* monitor the adsorption and desorption processes of the surfactant STAC molecules on the sensor surface. OWLS is a surface-sensitive technique utilizing a planar optical waveguide chip with a single coupling grating. The base of the waveguide chip is an 8 mm × 16 mm glass substrate. Using the sol–gel technique, a TiO_2-SiO_2 waveguide layer was created on this glass substrate (OW2400 sensor chip, MicroVacuum Ltd.). In the center of the chip, a shallow 1 mm wide optical grating was formed within the waveguide layer. The grating on the optical chip was illuminated by a He-Ne laser beam with a wavelength of 632.8 nm. This laser beam coupled through the grating generates an evanescent electromagnetic field that can probe changes in the refractive index near the optical waveguide surface (within a penetration depth of approximately 100–200 nm) [46]. The applied sensor chips support the 0th-order TE and TM waveguide modes. Photodiode detectors were positioned at both ends of the sensor chip. These detectors measured the intensity of light coupled into the waveguide while adjusting the angle of incidence of the illuminating laser beam. The grating equation was employed to calculate the effective refractive index value based on the measured coupling resonant angle [71]. By applying the mode equations, the refractive index and thickness of the adsorbed layer can be determined from the measured values, enabling the calculation of the adsorbed surface mass density using de Feijter's formula [71,72]. The sampling time for the measurements was set to 13 s. During the measurement process, the solution is directly applied to the surface of the waveguide sensor. The liquid cuvette and the injected solution entered through an injection port on top of the cuvette. A peristaltic pump was used to maintain a liquid flow rate of 1 μl/s into the cuvette [72].

The OWLS sensor chip was thoroughly cleaned before each measurement. Chips were soaked in dihydroxy(dioxo)chromium for 3 s and then rinsed with Milli-Q water (MQ, ultra-pure water). Subsequently, they were immersed in a 0.5 M potassium hydroxide (KOH) solution and rinsed with MQ water. The chip was sonicated in MQ water eight times for 5 min, after each cycle, the water was changed to a fresh one. For the drying process, nitrogen gas was utilized. Dried chips were left in MQ water overnight (for faster OWLS baseline saturation) until the measurements were done on the next day. During the OWLS measurement, the baseline was recorded in MQ water for approximately 10 min. Subsequently, a 0.01 mM STAC (Sigma-Aldrich Chemie GmbH, Darmstadt, Germany, catalog number: 53112-10G) solution was pumped into the OWLS cuvette and allowed to interact with the surface for 40 min. The reversibly adsorbed STAC was washed off with water. After, 0.1 mM STAC solution was pumped onto the surface for 40 min. In the next step, the excess STAC was again washed off with water for 40 min. Finally, the 1 mM STAC solution was pumped into the cuvette and then washed off with water.

2.2. QCM instrument and related protocols for monitoring the surface assembly of STAC layers from bulk solutions

Besides the OWLS, a QCM instrument, the so-called QCM-I (QCM with impedance measurement by MicroVacuum Ltd. (Budapest, Hungary)), was used to independently measure the formation of the STAC layers using the concentrations and times mentioned above. QCM sensors with a thin coating of waveguide film were employed (QCM TiAuTiSi chips, resonant frequency 5 MHz). Variations in surface adsorbed mass, such as adsorption or desorption of molecules on the crystal surface, result in measurable changes in the frequency and dissipation of the oscillation. An impedance (or admittance) spectrum is obtained to measure the resonance frequency and dissipation outputs [50].

First, we rinsed the chips with MQ water, then propanol, then MQ water, propanol, and finally MQ water again. Next, we soaked the chips in Roche Cobas Cleaner solution (Roche) for 5 min. After, we soaked them in a 2 % (v/v) Hellmanex III solution for another 5 min. Then thoroughly washed the chips with MQ water, and dried with N_2 flow. Finally, we place the QCM sensors on a metal tray and put the tray into an ozone cleaner (Microvacuum Ltd.) for 15 min. During the QCM measurement, we used exactly the same protocol as in the OWLS measurements. QCM data were analyzed by the NBS-QCManalysis software

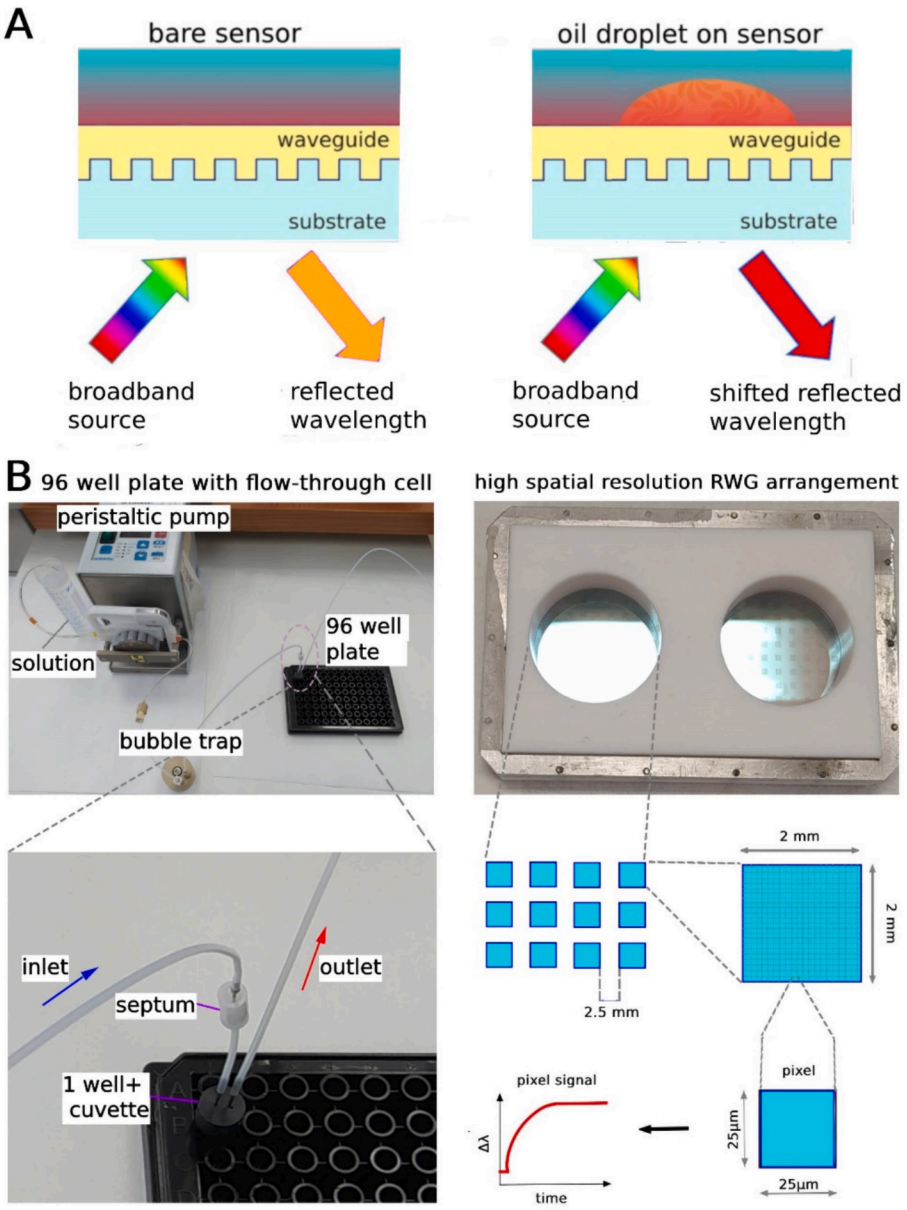

Fig. 1. **A** Schematic illustration of the working principle of RWG biosensor. Each waveguide sensor on the RWG plate is illuminated by a broadband light and as soon as a droplet adsorbs on the surface, the reflected wavelength is changed. This change in the detected wavelength leads to sensor signal shifts. **B** The images of two versions of RWG biosensors are illustrated. 96-well plate format detected the monolayer formation of the surfactant. A cuvette was attached to the conventional Epic plate with a septum, through which we pumped the samples. Excess material is discharged through the outlet. The oil droplet motion experiment occurred in the custom-made polytetrafluoroethylene (PTFE) well on an RWG biosensor. RWG biosensors can detect individual kinetic curves by the separated pixels of the sensor surface. The motion of the oil droplet induced the wavelength shift change on the biosensor.

using the Kelvin–Voigt model [50].

2.3. *RWG sensors and related protocols for monitoring surfactant self-assemblyand organic droplet motion*

The RWG-based Epic (Corning Inc., Corning, NY, USA) devices usually operate with 96- or 384-well Society for Biomolecular Screening (SBS) standard format biosensor microplates. RWG sensor units are made from the glass bottoms and Nb_2O_5 waveguide film deposited on a thicker glass substrate with etched coupling gratings of the cell assay microplates. The bottom of the waveguide was illuminated with 825–840 nm wavelength light, and the resonance wavelength was coupled into the Nb_2O_5 waveguide layer at sensor areas through the coupling gratings incorporated between the glass substrate and the waveguiding film. Only the specific resonant wavelength could propagate through a series of total internal reflections in the waveguide and form an evanescent field above the sensor (see Fig. 1**A**). This field was determined as the exponentially decaying electromagnetic field generated when the light was reflected from the waveguide-aqueous cover boundary and has a penetration depth of 150 nm. The sensor detected the change in RI of the close vicinity of the surface of the waveguide. After a short propagation distance inside the waveguide, the incoupled resonance wavelength was outcoupled by the same grating and illuminated a CCD camera. The resonance wavelength depends on the refractive index of the layer above the sensor. Since the CCD camera can detect the image of the outcoupled signal, the image of the refractive index distribution near the sensor surface can be obtained. The device monitors the changes in resonant wavelength ($\Delta\lambda$) with a time resolution of 3 s.

Two versions of the RWG biosensor were applied in our

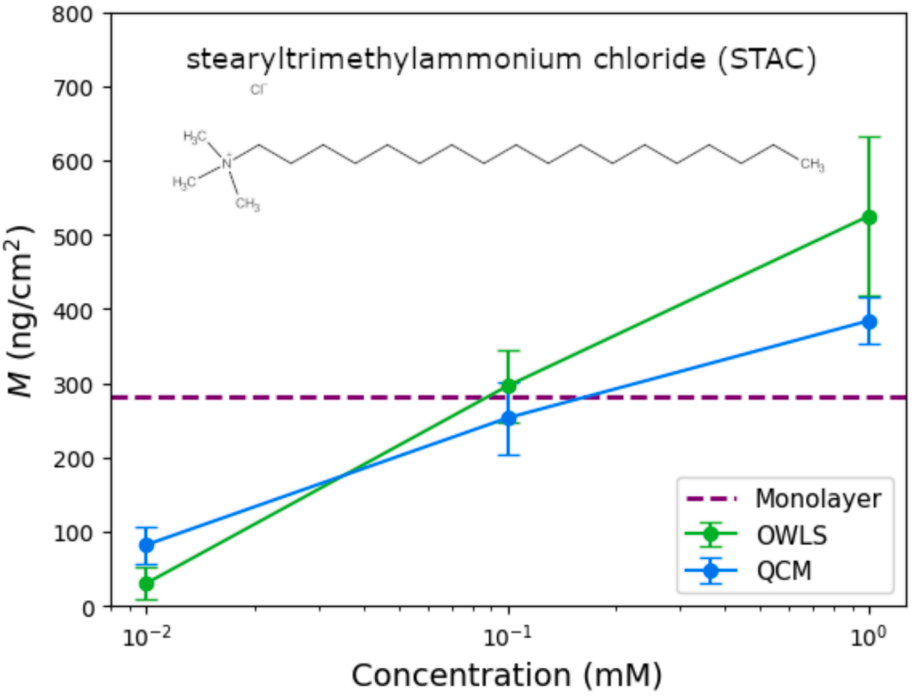

Fig. 2. Surface adsorbed mass densities of STAC layers from OWLS and QCM measurements at various bulk concentrations. The inset shows the structure of a STAC molecule. The dashed lines are the estimated monolayer coverage based on refs. [74,75] The top drawing indicates the structure of the adsorbed STAC layers at various bulk concentrations.

measurements (Fig. 1**B**). The surfactant adsorption and monolayer formation were studied with an Epic BT biosensor using a 96-well plate. A flow-through liquid cell fitting into the wells was designed, through which we passed our samples through a septum at a flow rate of 1 μl s^{-1}. In contrast, the droplet motion was measured with the Epic Cardio RWG sensor. The Epic Cardio biosensor has a spatial resolution of 25 μm, while the Epic BT has 90 μm. As a result, the Epic Cardio biosensor can detect the surface adhesions of single living cells [45,47,69,73], and it is an excellent candidate for monitoring the molecular-scale surface effects during droplet motion. Of note, the RWG-based Cardio biosensor operates similarly to the Epic BT biosensor, but can only simultaneously monitor 12 sensors of a 384-well biosensor microplate. Only the sensor glass bottoms (inserts) and the biosensor microplates without the plastic wells were used here. It is important to emphasize that the EPIC Cardio sensor records 12 × 80 × 80 kinetic curves simultaneously due to large lateral resolution of each of the 12 RWG sensor units (each having 80 × 80 measured pixels in the 2 × 2 mm^2 area).

A STAC (Sigma-Aldrich) water solution with various concentrations (1 mM, 0.1 mM, and 0.01 mM) was used in the Epic biosensor and Petri dish experiments. Since the STAC is a quaternary ammonium salt, the headgroup has a positive charge irrespective of the pH. In the Epic biosensor, 1 mM water solution of STAC (Sigma-Aldrich) was used. The organic solution containing 5 mM iodine (I_2) (Sigma-Aldrich) solution of nitrobenzene (Thermo Fisher Scientific) saturated with potassium iodide (KI) (VWR International) was used for droplet motion measurement. At room temperature (23±0.5 °C), a nitrobenzene droplet was placed in an aqueous phase into the RWG biosensor plate and the surface of the Petri dish.

3. Results and discussion

3.1. Characterization of STAC adsorption at different concentrations using OWLS and QCM

The adsorption properties of STAC molecules on the substrate were studied using OWLS and QCM sensors at 0.01, 0.1, and 1 mM concentrations. The motivation for the applications of these concentrations was that only a high concentration of STAC (1 mM) was used in the droplet motion experiments reported in the literature [6,7,16–25,8–15], and prior works supposed a compact self-assembled monolayer at this concentration. Of note, the employed techniques could not characterize the molecular layer buildup, only the droplet motion, and the examination of lower concentrations is completely missing in the literature. The main results of our OWLS and QCM experiments are shown in Fig. 2. Based on the surface density of the STAC (4.9 molecules nm^{-2}), we estimated the amount of STAC for a compact monolayer (282 ng cm^{-2}) [74,75]. We found that at low STAC concentration (0.01 mM), there is no compact monolayer formation (OWLS and QCM measurements provided the surface coverage of 30 and 80 ng cm^{-2}, respectively). Increasing the surfactant concentration, the adsorbed amount increases with a saturation trend. At a moderate STAC concentration (0.1 mM), the absorbed amount (OWLS: 300 ng cm^{-2} and QCM: 250 ng cm^{-2}) indicates nearly complete monolayer formation. However, at a high STAC concentration (1 mM) used in other studies in the past, the adsorbed amount (OWLS: 525 ng cm^{-2} and QCM: 380 ng cm^{-2}) is significantly greater than the amount estimated from the surface density of STAC (see dashed line in Fig. 2). This indicates the formation of a partial bilayer (multilayer) on the surface of the substrate. This hypothesis is reasonable since the apolar carbon chain can interact via van der Waals interaction.

It is important to emphasize that for highly ordered adsorbed layers, the OWLS technique can indicate layer anisotropy (birefringence), as predicted by theoretical calculations and demonstrated to various self-assembled structures [48–50,67,75]. In short, by applying the homogeneous and isotropic layer model for the measured OWLS data, one can calculate the quasi-isotropic thickness and refractive index of the adsorbed films. These values are under or overestimated, depending on the sign of the anisotropy. For the STAC layers, a heavily overestimated (around 1.9–2) layer refractive index was obtained (see SI Fig. S1) indicating negative birefringence (the layer refractive index is larger parallel with than perpendicular to the surface, ordinary RI is larger than extraordinary). However, the OWLS can predict the true layer thickness

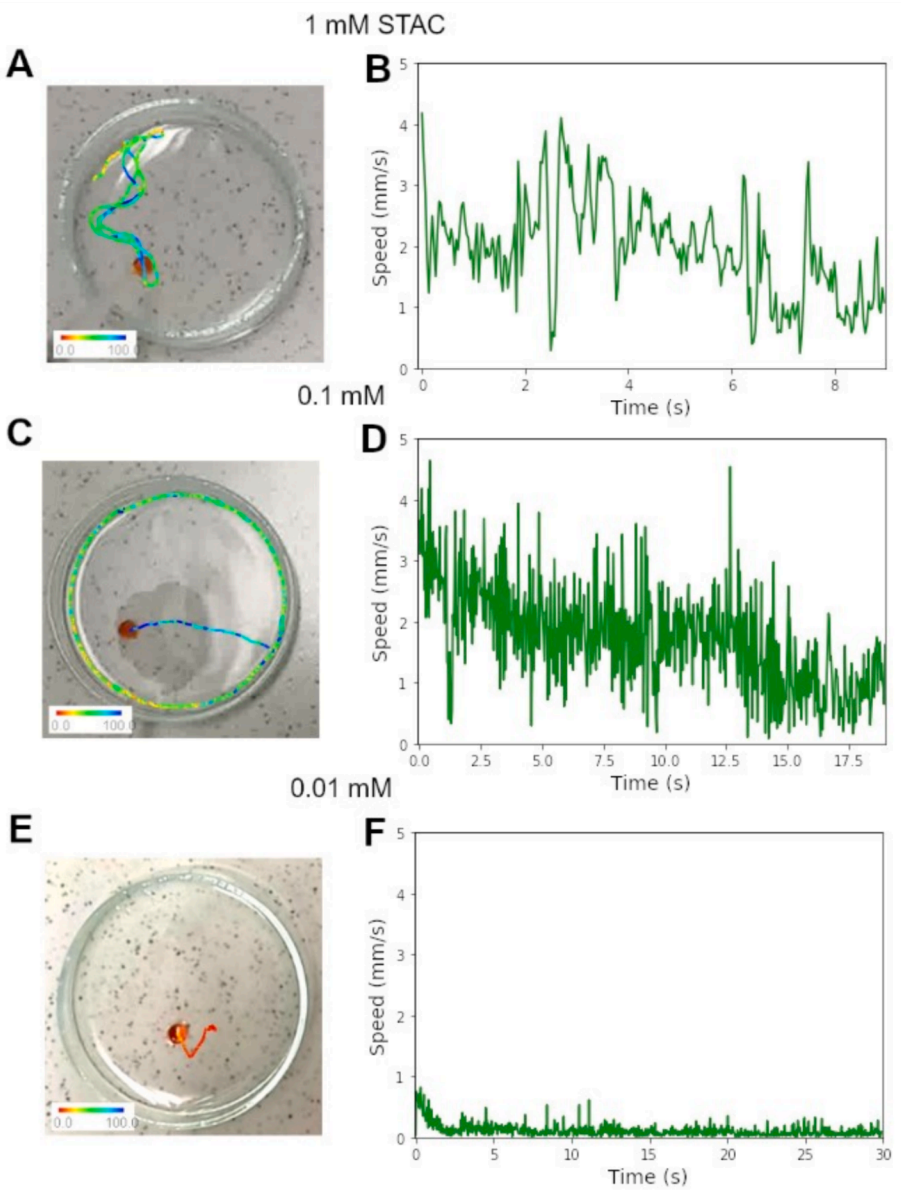

Fig. 3. Mode-switching in the motion of an organic droplet (30 μL) containing 5 mM iodine solution of nitrobenzene saturated with potassium iodide by varying the concentration of STAC in the water phase, **A, B** 1 mM, **C, D** 0.1 mM, and **E, F** 0.01 mM.

by taking a reasonable averaged RI for the films, even for anisotropic films. These values are shown in the SI file, and a reasonable agreement between QCM and OWLS data was found. (see SI Figs. S1 and S2) Of note, the larger OWLS mass per unit area at high concentrations might also be in connection with the optical anisotropy. Theoretical calculations predict that for negatively birefringent films, the OWLS overestimates the surface adsorbed mass density [76].

3.2. Mode-switching of the droplet motion

After investigating the STAC layer buildup and before investigating the STAC removal and motion of the organic droplet on the RWG sensor surface, we conducted droplet motion experiments in a glass bottom Petri dish using the above three STAC concentrations (1 mM, 0.1 mM, and 0.01 mM). We used borosilicate Petri dishes with a diameter of 52 mm without any surface cleaning or treatment. In a typical experiment, the water solution of STAC was transferred to the Petri dish, creating a 0.5 cm liquid layer. After 20 min, 30 μL of nitrobenzene droplet was placed on the glass substrate. The droplet motion was recorded using a digital camera (Samsung X4).

The motivation for these preliminary experiments was that only a high concentration of STAC (1 mM) was used in the droplet motion experiments reported in the literature [6,7,16–25,8–15], no data is provided at lower concentrations. At the high concentration of STAC (1 mM), the droplet exhibited random motion, having an average speed of 1.97 mm s^{-1} with a high standard deviation (0.81 mm s^{-1}, Fig. 3A and SI Video). The droplet motion can be explained by the difference in the contact angle of the oil droplet [13]. The contact angle at the front becomes lower than that of the rear, which originates from the difference in the surface concentration of STAC. The adsorbed STAC is easily removed from the solid surface to the organic phase containing I_2. Therefore, after passing the oil droplet, the surface concentration of STAC decreases, which is the origin of the driving force of the droplet motion. At a moderate STAC concentration (0.1 mM), the motion mode changed to the directional (straight) one. However, the average speed (1.76 mm s^{-1}) and the standard deviation (0.85 mm s^{-1}) remained the same compared to the motion using high STAC concentration (Fig. 3B and SI Video). We did not observe any motion at the low surfactant

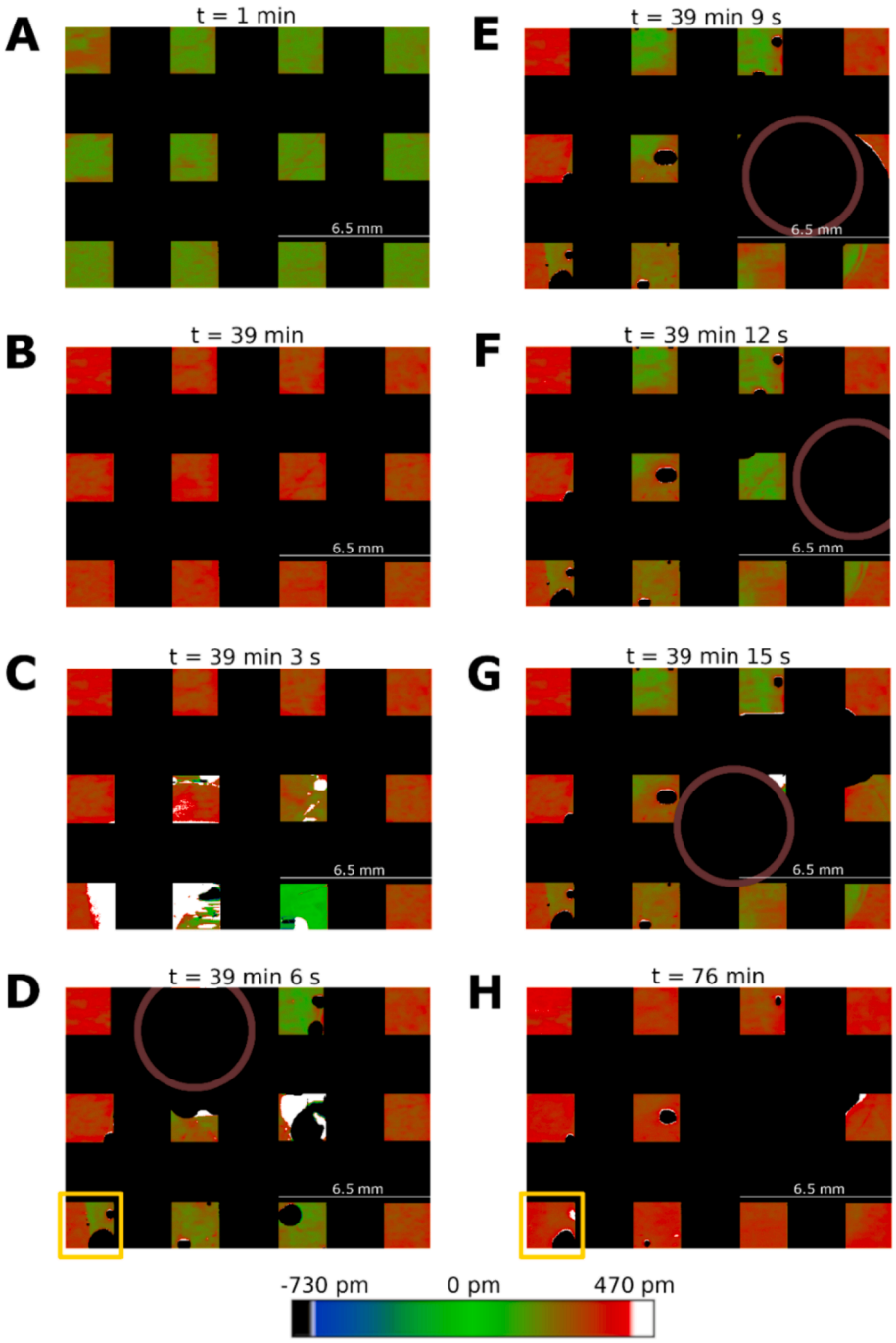

Fig. 4. 12 RWG sensors on the plate are shown and each sensor provides multiple data points, resulting in a total of 12 × 80 × 80 independent kinetic curves from the independent pixels located on each of the 12 sensors. **A**, The surface of the sensor without chemicals showed a green color. **B**, The color changed to red by the adsorption of the STAC molecular layer. **C**, Enters the drop (indicated by a brown circle) on the STAC layer. **D**, The drop goes through the STAC layer and picks up materials from the surface. **E**, The droplet changes direction. **F**, Smaller droplets separate. **G**, The droplet returns **H**, The drop stops, and STAC covers the surface again. (For interpretation of the references to color in this figure legend, the reader is referred to the web version of this article.)

concentration (0.01 mM) (Fig. 3C and SI Video).

The mode-switching of the organic droplet motion on the substrate observed in the experiments can be explained by the following arguments. The fundamental mechanism of droplet motion is the dynamics of the contact line, which is a triple line among an oil droplet, STAC aqueous solution, and solid substrate. The contact line of the droplet is more strongly pulled toward the aqueous phase if the concentration of absorbed STAC molecules is high. For the low STAC concentration, the amount of STAC molecules absorbed to the substrate should be smaller, and thus, the force generated at the droplet surface cannot move the droplet. Therefore, the droplet exhibits the rest state. For the moderate STAC concentration, more STAC molecules are absorbed at the substrate surface, which leads to a higher driving force. Once the droplet moves slightly in a direction determined by fluctuation, the front side of the droplet touches the substrate with higher concentration, and the front is strongly pulled in the moving direction. Therefore, the droplet exhibits a straight motion. In the case of higher STAC concentrations, the force that pulls the droplet surface towards the aqueous phase becomes stronger. Therefore, the droplet is pulled in several directions, resulting in the dynamic deformation of the droplet (SI Video). The droplet that

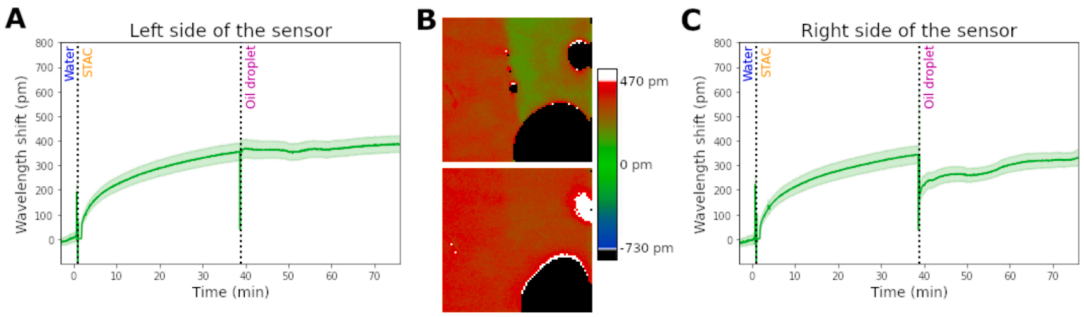

Fig. 5. Representative kinetic curves of STAC layer formation recorded by RWG Cardio sensor. The average kinetic signal of one sensor was presented, which were averaged the various sensor part pixel signals **A**, Monolayer of STAC builds up on the left side of the sensor. The nitrobenzene droplet did not reach this sensor area. **B,** Biosensor images demonstrate the droplet motion. The black area shows derived smaller droplets, which the original oil droplet leaves behind. The red surface is the STAC-covered surface, while the green color represent the area where the STAC was picked up from the surface. The size of the sensor is 2 × 2 mm. **C**, The nitrobenzene droplet passed through the STAC-covered monolayer on the right side of the sensor. (For interpretation of the references to color in this figure legend, the reader is referred to the web version of this article.)

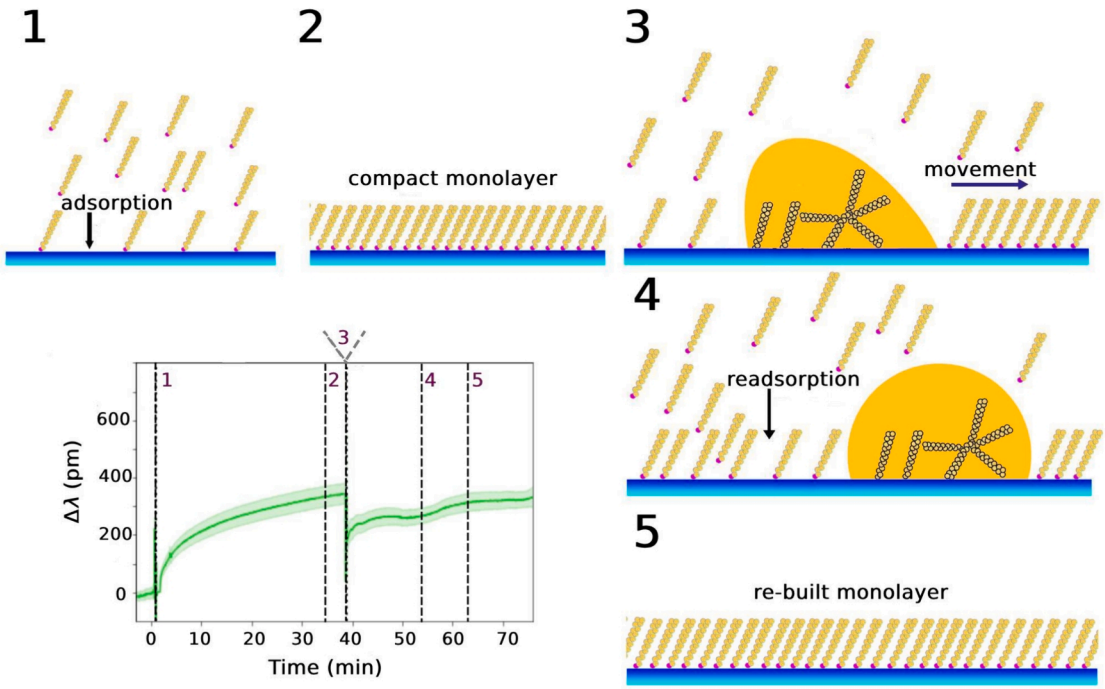

Fig. 6. Illustration of the possible adsorption of the STAC molecules on the sensor surface. **1**, The STAC molecules adsorption on the sensor surface. **2**, The hydrophobic carbon chains of STAC are oriented outwards, while the polar head is attached to the sensor surface. **3**, The droplet desorbs the STAC molecules from the surface. **4**, After the droplet has picked up the STAC molecules, the STAC molecules in the solution are adsorbed onto the surface. **5**, A new saturated monolayer is formed on the surface. The kinetic signals for each process are shown in the inset.

dynamically changes its shape can change its direction of motion since the force acting at the local surface of the droplet is not coherent. Therefore, in such a case, the center of mass of the droplet also shows a random motion.

3.3. Kinetic analysis of self-catalyzed droplet motion and STAC layer dynamics by high spatial resolution RWG sensor

Before investigating the droplet motion on the sensor surfaces, we examined the STAC build-on process on the same surface using the 96 well plate fit flow-through cuvette and direct injection. For the details, see SI Fig. S3. Of note, at this surface, a close to monolayer coverage was achieved at the highest concentration. The slightly lower mass (around 190 ng cm^{-2}) compared to the OWLS and QCM measurements, we attribute to the different behavior of self-assembly on the SiO_2-TiO_2 and Nb_2O_5 surfaces.

The self-propelled motion of the nitrobenzene droplet in STAC was monitored in real time by the RWG-based Cardio biosensor to record the kinetics of droplet motion. The typical experimental curves for STAC layer formation and regeneration after droplet motion are shown in Fig. 4. The baseline was recorded in water. Then, the STAC solution was pipetted into the well. Once the STAC layer reached saturation, a nitrobenzene drop was added into the well, exhibiting random motion on the STAC layer with an average speed of 13.4 mm s^{-1}. The motion lasted around 1 min, and after that, the droplet stuck to the surface. Kinetic information on monolayer formation was collected for 20 min.

Fig. 5**B** indicates the wavelength shift pattern on a biosensor pixel affected by drop after the nitrobenzene droplet passes through the

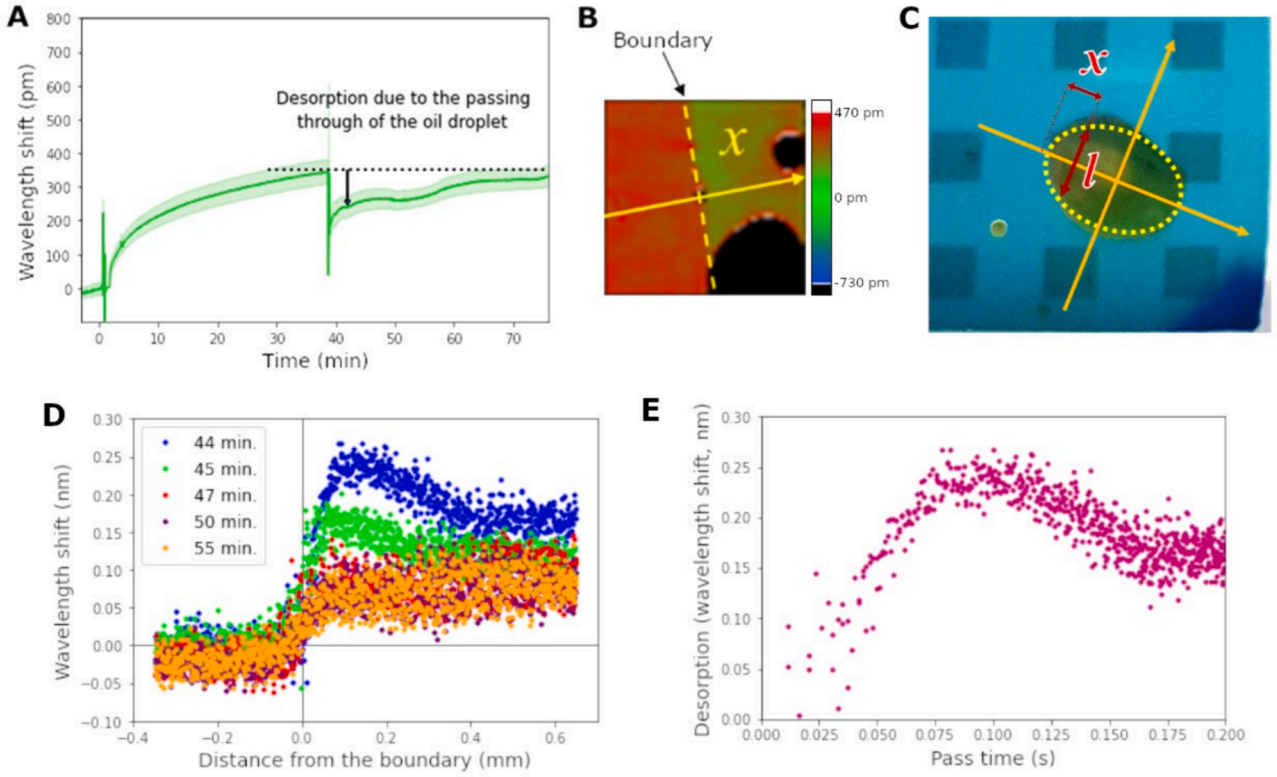

Fig. 7. Estimation of the desorption rate of STAC due to the droplet motion. **A**, Representative kinetic curves of STAC adsorption and desorption due to the droplet motion recorded by RWG biosensor. **B**, Image of the biosensor right after the nitrobenzene droplet passed through the STAC-covered monolayer on the right side of the sensor. The dashed line shows the passage of the edge of the droplet. **C**, Photograph of droplet motion. The droplet was fitted with an ellipse illustrated broken yellow line. **D,** Desorbed amount of STAC in the function of the distance measured from the passage of the edge of the droplet. **E**, The jump of wavelength shift (44 min) depends on the time length passing the oil droplet. (For interpretation of the references to color in this figure legend, the reader is referred to the web version of this article.)

Table 1
Comparison of the advantage and disadvantage of surface-sensitive label-free techniques which can potentially detect changes at droplet interfaces.

Detection technique	sampling time	lateral resolution	advantage	disadvantage	references
OWLS	1–10 s	No lateral resolution	real-time detection, submonolayer sensitivity detection of anisotropy	single sensor	[86,90]
Imaging SPR	10 s	lateral resolution of less than 2 μm	high lateral resolution	fixed metal interface	[91,92]
SPR	few seconds	no lateral resolution	real-time detection, submonolayer sensitivity	no anisotropy detection	[90,93]
QCM	6.2 s	no lateral resolution	real-time detection, submonolayer sensitivity, viscoelastic layer properties	high sensitivity to vibration, mechanical noises	[82,85,90]
Ellipsometry	1 to 100 s	no lateral resolution	sensitivity to thicker layers	Illumination through bulk liquid,may scatter the light and disturb the signal	[89]
Imaging ellipsometry	1 s	high lateral resolution, 0.5 μm	high lateral and temporal resolution	Illumination through bulk liquid, may scatter the light and disturb the signal	[85,87]
Total internal refraction ellipsometry	4 s	no lateral resolution	high temporal resolution	droplet may scatter the light and disturb the signal	[88,89,94]
resonant waveguide grating (RWG)	3 s	resolution 80 μm	high temporal resolution	low lateral resolution	[95]
Single-cell RWG	3 s	high lateral resolution, 25 μm	high lateral and temporal resolution	not available commercially	[69,96]

domain (upper picture) and at the end of the observation (bottom picture). Fig. 5**A** shows the characteristic kinetic curve of the adsorption of the STAC on the surface of the biosensors. Before adding the droplet, the STAC monolayer built up and uniformly covered the surface of the biosensor with the estimated desorption rate coefficient of 1.20×10^{-3} s^{-1} (**Fig. S5**). In Fig. 5**B**, after the addition of the nitrobenzene droplet, the droplet started to move, and this motion was fueled by the partial removal of surfactant molecules from the monolayer driven by the dissolution of the STAC due to the interaction of the organic droplet with the amphiphilic molecules of the STAC. In the case of the RWG sensor measurements, there was no washing step, as the STAC monolayer was stripped off only by the droplet passing through the sensor. Biosensor

images present the average wavelength shift in the domains unaffected by the droplet motion. On the other hand, Fig. 5**C** shows the kinetic curve in which a droplet moved through the domain. Once a droplet passed the domain, the signal dropped by one-third, indicating the desorption of the STAC molecules due to their dissolution in the nitrobenzene. This amount corresponds to 72 ng cm^{-2} in this representative experiment. For the conversion of wavelength shift to surface adsorbed mass, see the SI. Of note, in repeated experiments this removed relative amount heavily fluctuated, reaching even 80 % in some cases. This is most probably in connection with the observed velocity fluctuations. We hypothesize that this amount can be inversely proportional to the speed of the droplet. We can observe that after the removal of STAC, the monolayer built up within ~20 min, because the STAC molecules floating in the liquid supernatant were able to re-adsorb onto the surface after the droplet had passed. A schematic diagram of the droplet movement is illustrated based on kinetic signals, as shown in Fig. 6. STAC molecules can be adsorbed onto the sensor surface by electrostatic interaction. The hydrophobic carbon chains of STAC align outwardly, while the polar head attaches to the sensor surface. The droplet causes the desorption of STAC molecules from the surface. Once the droplet dissolves the STAC molecules, the STAC molecules from the solution are readsorbed onto the surface. This results in the formation of a new saturated monolayer on the surface.

The dissolution of STAC into the oil phase has been shown qualitatively by separate experiments of the droplet motion, for example contact angle of water on the glass plate before and after soaking into the oil phase [13]. Our results enable us to quantitatively estimate the dissolution/transfer rate of STAC into the oil phase. Fortunately, the oil passed through half of the sensor (see Fig. 5). By analyzing the results of the sensor, the distance dependency from the boundary can be realized. The decreasing value just after passing through the droplet was measured around the boundary and plotted against the distance from the boundary (Fig. 7). It indicates that the values much decreased near the boundary, and they gradually recovered with time over a few minutes. The position dependency originates from the time length passing through the oil droplet. Near the edge of the droplet, the pass length of the droplet becomes shorter rather than the center. Thus, the time length of soaking in the oil becomes also short. We estimate the time length depending on the distance from the boundary by assuming the droplet shape as an ellipse, and the droplet moved with a constant speed estimated as 13.4 mm s^{-1} from a separate Video observation under the same experimental condition. The shape of the droplet was fitted with an ellipse whose long axis was $a = 5.2$ mm and short was $b = 4.1$ mm. Thus, the pass length (l) can be calculated as the function of the distance from boundary (x) as follows:

$$l(\mathrm{x}) = b\sqrt{1-\frac{(x-a/2)^2}{(a/2)^2}} = 4.1\sqrt{1-\frac{(x-2.6)^2}{2.6^2}}$$

Due to the droplet moving with a constant speed, v, the time period exposed to the droplet can be estimated by l/v. The slope at the short-time region was estimated as 1.46×10^{-6} g s^{-1} cm^{-2}, and the value approached 7.93×10^{-8} g cm^{-2}. Based on the simple model [77], the former corresponds to $\left(\phi(0) - \frac{k_a}{k_d}\right)k_d$ and the latter $\left(\phi(0) - \frac{k_a}{k_d}\right)$, where $\phi(0)$ is the initial value, k_a is the adsorption rate, and k_d is the desorption rate. Therefore, we can estimate the desorption rate into the oil phase as 18.4 s^{-1}. For the detailed calculations see the SI.

In analyzing the experiment results, it is important to consider the reproducibility of the measurements. Based on the measurements, the amount of STAC adsorbed on the biosensor surface at higher STAC concentrations (1 and 0.1 mM) was reproducible with ~10 % error. However, the amount of desorbed surfactant due to the droplet motion is influenced by the contact time of the organic droplet with a surface region. This contact time is affected by the size and speed of the droplet. Although the droplet volume was constant in the experiments, the speed fluctuated widely. The maximum speed change observed was 3.71 mm s^{-1} over 0.1 s (Fig. 2). Consequently, the amount of STAC removed due to droplet motion is influenced by the local speed of the droplet at the given contact region with the surface. If the local speed is high, the contact time of the droplet with the surface is shorter (thus, the desorbed amount of STAC is low) and *vice versa*. Therefore, the reproducibility of the droplet motion measurements is highly affected by this velocity (speed) fluctuation of the droplet.

4. Conclusions

Here, we employed optical waveguide sensors to in-situ monitor the motion of self-propelled organic droplets and the underlying driving processes with molecular-scale resolution. We utilized RWG, QCM, and OWLS devices to investigate the kinetics of the self-assembled monolayer formation of the STAC surfactant, which plays a key role during the self-propelled motion. The surface adsorption–desorption of STAC molecules and the orientation inside the self-assembled films were all monitored at various STAC concentrations. In contrast to previous works, we first employed lower bulk STAC concentrations than the concentration, leading to the formation of compact STAC monolayers, Moreover, we discovered that at 1 mM concentration, the formed STAC layer has a multilayer structure on certain surfaces. This effect was completely overlooked in the literature. Based on these systematic investigations, we discovered a mode-switching effect in the droplet motion, strongly depending on the bulk STAC concentration, and analyzed the speed fluctuations during the droplet motion. Uniquely, both the droplet motion and the kinetic changes in the STAC layer were investigated *in situ* using a high spatial resolution RWG device. The regeneration kinetics of the self-assembled monolayer at surface areas visited by the moving droplet were also revealed and studied for the first time. By combining the capabilities of RWG, QCM, and OWLS, we could verify that during the motion of a nitrobenzene droplet on the substrate surface decorated with a self-assembled monolayer of STAC molecules, there is a removal of the surfactants driven by the dissolution of STAC molecules in the organic phase. RWG and OWLS measurements indicated that the adsorbed amount of the STAC molecules is around the monolayer coverage at 0.1 mM bulk STAC concentration and slightly exceeds this at 1 mM concentration. Of note, a slightly lower than monolayer coverage was observed in the RWG experiments at 1 mM concentration, what we attribute to the different surface properties of the substrates used for STAC adsorption. From the RWG measurements we concluded that the droplet removed around one-third of the adsorbed amount with a rate of 18.4 s^{-1}, which fueled the self-propelled motion of the nitrobenzene droplet. Of note, due to the fluctuation in the velocity, this value is presumably heavily fluctuating, too. This study can help to design a similar self-propelled system at a solid–liquid interface by exactly quantifying the adsorbed and removed amount of the surfactants and their build-up kinetics.

It is important to emphasize that traditional methods for characterizing the molecular-scale self-assembly processes do not effectively capture self-driven droplet motion and the underlying molecular-scale interactions in a single experiment. Table 1 shows a comparison of surface-sensitive techniques typically available today, highlighting the advantages and disadvantages of these techniques in the present field.

Interfacial processes are often characterized by optical methods such as ellipsometry, OWLS, SPR, acoustic wave sensors, and quartz crystal microbalance (QCM) [78–80]. However, while OWLS, QCM, SPR, and ellipsometry provide advantages such as high sensitivity and real-time monitoring, their missing lateral resolution makes them less suitable for applications requiring detailed spatial information on molecular scale events [43,81–84]. For example, the resonance frequency and dissipation shifts at QCM were monitored with a time resolution of 6.2 s for each selected overtone [50,85], while the time resolution 14 s at OWLS [86] and few seconds at SPR [87]. This would make it difficult to

follow the motion of droplets due to the limited time and lateral resolution. Of note, imaging ellipsometry is favored for applications requiring high lateral resolution and precise characterization of thin film properties on surfaces. Although the liquid interface with moving droplets may scatter the light, and this effect could destroy the optical signal in standard elliposometry arrangements [88–90]. We emphasize that achieving high lateral resolution in novel label-free (bio)sensors is crucial for accurately characterizing interfacial processes and detecting subtle changes in surface properties or macroscopic interactions [50,69,79].

Our proof of principle work has a potential relevance in other fields, too. Understanding monomolecular layer reconstitution is crucial for self-structuring [26,27] and self-healing materials [28], as well as pharmaceutical formulations [29–31] aiming to create such layers. The recovery dynamics of surface layers at the solid–liquid interface are also significant for advancing self-cleaning technologies [31,35,36]. Both macroscopic and nanoscale movements hold promise for future studies in soft robotics [97–101], point-of-care testing [102,103], and powerless actuation [104,105], utilizing the motion generated by a rotating droplet within fluidics. Therefore, the methodology introduced here, for simultaneously monitoring macroscopic motion and the underlying molecular-scale effects in a label-free and non-invasive manner, could be adapted to other research fields on advanced materials, functional coatings, and novel ways of actuation. Potential directions for future research could also involve expanding the analysis to different types of surfactants to gain a deeper understanding of universal self-organization mechanisms and organic droplet motion. Additionally, comparing results with alternative surface analysis techniques could better illuminate the differences in the structure of the self-assembled surface layers. Especially, the discovered multilayer formation and its effects on droplet motion could be investigated in more detail by modifying the RWG surfaces to obtain over the monolayer STAC films. Concerning the RWG sensors, these experiments would benefit from a much larger homogeneously covered sensor area (several cm) with significant lateral resolution. Instrumental development in the direction of precise temperature control would be also useful to be able to perform more sophisticated experiments.

CRediT authorship contribution statement

Eniko Farkas: Writing – review & editing, Writing – original draft, Visualization, Validation, Supervision, Investigation, Formal analysis, Data curation. **Kinga Dóra Kovács:** Visualization, Validation, Software, Investigation, Funding acquisition, Formal analysis, Data curation. **Inna Szekacs:** Writing – review & editing, Validation, Supervision, Project administration. **Beatrix Peter:** Writing – review & editing, Validation, Supervision, Resources, Project administration, Funding acquisition. **István Lagzi:** Writing – review & editing, Validation, Supervision, Resources, Project administration, Investigation, Funding acquisition, Data curation, Conceptualization. **Hiroyuki Kitahata:** Writing – review & editing, Writing – original draft, Supervision, Methodology, Investigation, Formal analysis, Data curation, Conceptualization. **Nobuhiko J. Suematsu:** Writing – review & editing, Validation, Supervision, Resources, Project administration, Investigation, Funding acquisition, Data curation, Conceptualization. **Robert Horvath:** Writing – review & editing, Writing – original draft, Resources, Project administration, Investigation, Funding acquisition, Formal analysis, Conceptualization.

Declaration of competing interest

The authors declare that they have no known competing financial interests or personal relationships that could have appeared to influence the work reported in this paper.

Data availability

Data will be made available on request.

Acknowledgements

The authors appreciate Prof. Satoshi Nakata for his helpful advice and discussion. This work was supported by the National Research, Development and Innovation Office of Hungary (K131425 and 146071), the National Research, Development, and Innovation Fund of Hungary under Grant TKP2021-EGA-02, TKP2021-EGA-04, HUN-REN Hungarian Research Network, and JSPS Japan-Hungary Bilateral Joint Research Project (JPJSBP 120213801). This project was supported by the János Bolyai Research Scholarship of the Hungarian Academy of Sciences (for B.P.). This work was supported by the KDP-2021 program of the Ministry of Innovation and Technology from the source of the National Research, Development and Innovation Fund.

Appendix A. Supplementary material

Supplementary material to this article can be found online at https://doi.org/10.1016/j.jcis.2024.07.236.

References

[1] E. Hilner, A.A. Zakharov, K. Schulte, P. Kratzer, J.N. Andersen, E. Lundgren, A. Mikkelsen, Ordering of the nanoscale step morphology as a mechanism for droplet self-propulsion, Nano Lett. 9 (2009) 2710–2714, https://doi.org/10.1021/nl9011886.
[2] A. Shioi, T. Ban, Y. Morimune, Autonomously Moving colloidal objects that resemble living matter, Entropy. 12 (2010) 2308–2332, https://doi.org/10.3390/e12112308.
[3] J. Wang, Nanomachines, Fundament. Appl. (2013), https://doi.org/10.1002/ange.201311274.
[4] T. Toyota, N. Maru, M.M. Hanczyc, T. Ikegami, T. Sugawara, Self-propelled oil droplets consuming "Fuel" surfactant, J. Am. Chem. Soc. 131 (2009) 5012–5013, https://doi.org/10.1021/ja806689p.
[5] T. Bánsági, M.M. Wrobel, S.K. Scott, A.F. Taylor, Motion and interaction of aspirin crystals at aqueous-air interfaces, J. Phys. Chem. B. 117 (2013) 13572–13577, https://doi.org/10.1021/jp405364c.
[6] A.K. Schmid, N.C. Bartelt, R.Q. Hwang, Alloying at surfaces by the migration of reactive two-dimensional islands, Science. 290 (2000) 1561–1564, https://doi.org/10.1126/science.290.5496.1561.
[7] T. Toyota, H. Tsuha, K. Yamada, K. Takakura, T. Ikegami, T. Sugawara, Listeria-like motion of oil droplets, Chem. Lett. 35 (2006) 708–709, https://doi.org/10.1246/cl.2006.708.
[8] M.M. Hanczyc, T. Toyota, T. Ikegami, N. Packard, T. Sugawara, Fatty acid chemistry at the oil-water interface: Self-propelled oil droplets, J. Am. Chem. Soc. 129 (2007) 9386–9391, https://doi.org/10.1021/ja0706955.
[9] T. Banno, T. Toyota, K. Asakura, Self-Propelled Motion of Micrometer-Sized Oil Droplets in Aqueous Solution of Surfactant, in: Prop. Uses Microemulsions, 2017: pp. 139–154. doi: 10.5772/67249.
[10] R. Seemann, J.B. Fleury, C.C. Maass, Self-propelled droplets, Eur. Phys. J. - Spec. Top. 225 (2016) 2227–2240, https://doi.org/10.1140/epjst/e2016-60061-7.
[11] M.D. Levan, Motion of a droplet with a Newtonian interface, J. Colloid Interf. Sci. 83 (1981) 11–17, https://doi.org/10.1016/0021-9797(81)90003-5.
[12] F. Brochard-Wyart, P.-G. De Gennes, Spontaneous motion of a reactive droplet, C. r. Acad. Sci. II. C. 321 (1995) 285–288.
[13] Y. Sumino, N. Magome, T. Hamada, K. Yoshikawa, Self-running droplet: Emergence of regular motion from nonequilibrium noise, Phys. Rev. Lett. 94 (2005) 1–4, https://doi.org/10.1103/PhysRevLett.94.068301.
[14] Y. Sumino, H. Kitahata, K. Yoshikawa, M. Nagayama, S.I.M. Nomura, N. Magome, Y. Mori, Chemosensitive running droplet, Phys. Rev. E. 72 (2005) 1–17, https://doi.org/10.1103/PhysRevE.72.041603.
[15] F.D. Dos Santos, T. Ondarquhus, Free-running droplets fabrice, Physcal Rev. Lett. 75 (1995) 2972, https://doi.org/10.1103/PhysRevLett.75.2972.
[16] P. Lazar, H. Riegler, Reversible self-propelled droplet movement: A new driving mechanism, Phys. Rev. Lett. 95 (2005) 1–4, https://doi.org/10.1103/PhysRevLett.95.136103.
[17] F. Brochard, Motions of droplets on solid surfaces induced by chemical or thermal gradients, Langmuir. 5 (1989) 432–438, https://doi.org/10.1021/la00086a025.
[18] K. John, M. Bär, U. Thiele, Self-propelled running droplets on solid substrates driven by chemical reactions, Eur. Phys. J. E. 18 (2005) 183–199, https://doi.org/10.1140/epje/i2005-10039-1.
[19] P. Nepomnyashchy, A. A.; Velarde, M. G.; Colinet, Interfacial Phenomena and Convection, in: Chapman Hall/CRC Gt. Britain, 2002: p. Chapter 3. doi: 10.1201/9781482296303.

[20] N. Magome, K. Yoshikawa, Nonlinear oscillation and ameba-like motion in an oil/water system, J. Phys. Chem. 100 (1996) 19102–19105, https://doi.org/10.1021/jp9616876.
[21] A. Shioi, K. Katano, Y. Onodera, Effect of solid walls on spontaneous wave formation at water/oil interfaces, J. Colloid Interf. Sci. 266 (2003) 415–421, https://doi.org/10.1016/S0021-9797(03)00672-6.
[22] K. Yoshikawa, T. Omochi, Y. Matsubara, H. Kourai, A possibility to recognize chirality by an excitable artificial liquid membrane, Biophys. Chem. 24 (1986) 111–119, https://doi.org/10.1016/0301-4622(86)80004-7.
[23] N.M. Kovalchuk, D. Vollhardt, Effect of substance properties on the appearance and characteristics of repeated surface tension auto-oscillation driven by Marangoni force, Phys. Rev. E. 69 (2004) 016307, https://doi.org/10.1103/PhysRevE.69.016307.
[24] J.I. Dupeyrat, E. Nakache, 205-direct conversion of chemical energy into mechanical energy at an oil water interface, Bioelectroch. Bioener. 5 (1978) 134–141, https://doi.org/10.1016/0302-4598(87)87013-7.
[25] T. Takahashi, H. Yui, T. Sawada, Direct observation of dynamic molecular behavior at a water/nitrobenzene interface in a chemical oscillation system, J. Phys. Chem. B. 106 (2002) 2314–2318, https://doi.org/10.1021/jp013447i.
[26] F. Jia, X. Peng, J. Wang, T. Wang, K. Sun, Marangoni-driven spreading of a droplet on a miscible thin liquid layer, J. Colloid Interf. Sci. 658 (2024) 617–626, https://doi.org/10.1016/j.jcis.2023.12.092.
[27] R.T. van Gaalen, C. Diddens, H.M.A. Wijshoff, J.G.M. Kuerten, Marangoni circulation in evaporating droplets in the presence of soluble surfactants, J. Colloid Interf. Sci. 584 (2021) 622–633, https://doi.org/10.1016/j.jcis.2020.10.057.
[28] Y. Ye, Y. Hong, Q. Liang, Y. Wang, P. Wang, J. Luo, A. Yin, Z. Ren, H. Liu, X. Qi, S. He, S. Yu, J. Wei, Bioinspired electrically stable, optically tunable thermal management electronic skin via interfacial self-assembly, J. Colloid Interf. Sci. 660 (2024) 608–616, https://doi.org/10.1016/j.jcis.2024.01.041.
[29] M.L. Sauleda, T.L. Hsieh, W. Xu, R.D. Tilton, S. Garoff, Surfactant spreading on a deep subphase: coupling of Marangoni flow and capillary waves, J. Colloid Interf. Sci. 614 (2022) 511–521, https://doi.org/10.1016/j.jcis.2022.01.142.
[30] N. Rezaee, J. Aunna, J. Naser, Marangoni flow investigation in foam fractionation phenomenon, Fluids. 8 (2023) 209, https://doi.org/10.3390/fluids8070209.
[31] S.V. Iasella, N. Sun, X. Zhang, T.E. Corcoran, S. Garoff, T.M. Przybycien, R. D. Tilton, Flow regime transitions and effects on solute transport in surfactant-driven Marangoni flows, J. Colloid Interf. Sci. 553 (2019) 136–147, https://doi.org/10.1016/j.jcis.2019.06.016.
[32] I. Kitamura, K. Oishi, M. Hara, S. Nagano, T. Seki, Photoinitiated Marangoni flow morphing in a liquid crystalline polymer film directed by super-inkjet printing patterns, Sci. Rep. 9 (2019) 1–11, https://doi.org/10.1038/s41598-019-38709-1.
[33] D. Lohse, Fundamental fluid dynamics challenges in inkjet printing, Annu. Rev. Fluid Mech. 54 (2021) 349–382, https://doi.org/10.1146/annurev-fluid-022321-114001.
[34] V. Nasirimarekani, O. Ramìrez-Soto, S. Karpitschka, I. Guido, Pattern formation under mechanical stress in active biological networks confined inside evaporating droplets, (2023) 1–31. http://arxiv.org/abs/2305.07099.
[35] J.G. Lee, L.L. Larive, K.T. Valsaraj, B. Bharti, Binding of lignin nanoparticles at oil-water interfaces: an ecofriendly alternative to oil spill recovery, ACS Appl. Mater. Interf. 10 (2018) 43282–43289, https://doi.org/10.1021/acsami.8b17748.
[36] D. Gupta, B. Sarker, K. Thadikaran, V. John, C. Maldarelli, G. John, Sacrificial amphiphiles: Eco-friendly chemical herders as oil spill mitigation chemicals, Sci. Adv. 1 (2015) 2–7, https://doi.org/10.1126/sciadv.1400265.
[37] M. Zarei, M. Zarei, Self-propelled micro/nanomotors for sensing and environmental remediation, Small. 14 (2018) 1–17, https://doi.org/10.1002/smll.201800912.
[38] M. Urso, M. Ussia, M. Pumera, Smart micro- and nanorobots for water purification, Nat. Rev. Bioeng. 1 (2023) 236–251, https://doi.org/10.1038/s44222-023-00025-9.
[39] Y. Ying, M. Pumera, Micro/nanomotors for water purification, Chem. - A Eur. J. 25 (2019) 106–121, https://doi.org/10.1002/chem.201804189.
[40] T. Ban, T. Yamagami, H. Nakata, Y. Okano, PH-dependent motion of self-propelled droplets due to marangoni effect at neutral pH, Langmuir. 29 (2013) 2554–2561, https://doi.org/10.1021/la3047164.
[41] T. Banno, R. Kuroha, T. Toyota, PH-sensitive self-propelled motion of oil droplets in the presence of cationic surfactants containing hydrolyzable ester linkages, Langmuir. 28 (2012) 1190–1195, https://doi.org/10.1021/la2045338.
[42] S. Thutupalli, R. Seemann, S. Herminghaus, Swarming behavior of simple model squirmers, New J. Phys. 13 (2011) 073021, https://doi.org/10.1088/1367-2630/13/7/073021.
[43] C. Chen, J. Wang, Optical biosensors: An exhaustive and comprehensive review, Analyst. 145 (2020) 1605–1628, https://doi.org/10.1039/c9an01998g.
[44] S. Daniel, M.K. Chaudhury, Induced by vibration, Society. 18 (2002) 3404–3407.
[45] Y. Fang, A.M. Ferrie, N.H. Fontaine, J. Mauro, J. Balakrishnan, Resonant waveguide grating biosensor for living cell sensing, Biophys. J. 91 (2006) 1925–1940, https://doi.org/10.1529/biophysj.105.077818.
[46] J. Vörös, J.J. Ramsden, G. Csúcs, I. Szendrő, S.M. De Paul, M. Textor, N. D. Spencer, Optical grating coupler biosensors, Biomaterials. 23 (2002) 3699–3710, https://doi.org/10.1016/S0142-9612(02)00103-5.
[47] N. Orgovan, B. Kovacs, E. Farkas, B. Szabó, N. Zaytseva, Y. Fang, R. Horvath, Bulk and surface sensitivity of a resonant waveguide grating imager, Appl. Phys. Lett. 104 (2014) 1–4, https://doi.org/10.1063/1.4866460.
[48] A. Saftics, G.A. Prósz, B. Türk, B. Peter, S. Kurunczi, R. Horvath, In situ viscoelastic properties and chain conformations of heavily hydrated carboxymethyl dextran layers: a comparative study using OWLS and QCM-I chips coated with waveguide material, Sci. Rep. 8 (2018) 1–14, https://doi.org/10.1038/s41598-018-30201-6.
[49] A. Saftics, S. Kurunczi, Z. Szekrényes, K. Kamarás, N.Q. Khánh, A. Sulyok, S. Bősze, R. Horvath, Fabrication and characterization of ultrathin dextran layers: Time dependent nanostructure in aqueous environments revealed by OWLS, Colloid Surface B. 146 (2016) 861–870, https://doi.org/10.1016/j.colsurfb.2016.06.057.
[50] A. Saftics, S. Kurunczi, B. Peter, I. Szekacs, J.J. Ramsden, R. Horvath, Data evaluation for surface-sensitive label-free methods to obtain real-time kinetic and structural information of thin films: A practical review with related software packages, Adv. Colloid Interf. Sci. 294 (2021) 102431, https://doi.org/10.1016/j.cis.2021.102431.
[51] J. Homola, Present and future of surface plasmon resonance biosensors, Anal. Bioanal. Chem. 377 (2003) 528–539, https://doi.org/10.1007/s00216-003-2101-0.
[52] J. Homola, H. Vaisocherová, J. Dostálek, M. Piliarik, Multi-analyte surface plasmon resonance biosensing, Methods. 37 (2005) 26–36, https://doi.org/10.1016/j.ymeth.2005.05.003.
[53] C. Boozer, G. Kim, S. Cong, H. Guan, T. Londergan, Looking towards label-free biomolecular interaction analysis in a high-throughput format: a review of new surface plasmon resonance technologies, Curr. Opin. Biotechnol. 17 (2006) 400–405, https://doi.org/10.1016/j.copbio.2006.06.012.
[54] N. Kanyo, K.D. Kovacs, A. Saftics, I. Szekacs, B. Peter, A.R. Santa-Maria, F. R. Walter, A. Dér, M.A. Deli, R. Horvath, Glycocalyx regulates the strength and kinetics of cancer cell adhesion revealed by biophysical models based on high resolution label-free optical data, Sci. Rep. 10 (2020) 1–20, https://doi.org/10.1038/s41598-020-80033-6.
[55] K.D. Kovács, M. Novák, Z. Hajnal, C. Hős, B. Szabó, I. Székács, Y. Fang, A. Bonyár, R. Horvath, Label-free tracking of whole-cell response on RGD functionalized surfaces to varied flow velocities generated by fluidic rotation, J. Colloid Interf. Sci. 599 (2021) 620–630, https://doi.org/10.1016/j.jcis.2021.04.091.
[56] E. Farkas, A. Szekacs, B. Kovacs, M. Olah, R. Horvath, I. Szekacs, Label-free optical biosensor for real-time monitoring the cytotoxicity of xenobiotics: A proof of principle study on glyphosate, J. Hazard. Mater. 351 (2018) 80–89, https://doi.org/10.1016/j.jhazmat.2018.02.045.
[57] B. Peter, E. Farkas, E. Forgacs, A. Saftics, B. Kovacs, S. Kurunczi, I. Szekacs, A. Csampai, S. Bosze, R. Horvath, Green tea polyphenol tailors cell adhesivity of RGD displaying surfaces: Multicomponent models monitored optically, Sci. Rep. 7 (2017) 1–16, https://doi.org/10.1038/srep42220.
[58] E. Farkas, D. Patko, N.Q. Khanh, E. Toth, F. Vonderviszt, R. Horvath, Self-assembly and structure of flagellin-polyelectrolyte composite layers: Polyelectrolyte induced flagellar filament formation during the alternating deposition process, RSC Adv. 6 (2016) 92159–92167, https://doi.org/10.1039/c6ra19010c.
[59] E. Farkas, D. Srankó, Z. Kerner, B. Setner, Z. Szewczuk, W. Malinka, R. Horvath, Ł. Szyrwiel, J.S. Pap, Self-assembled, nanostructured coatings for water oxidation by alternating deposition of Cu-branched peptide electrocatalysts and polyelectrolytes, Chem. Sci. 7 (2016) 5249–5259, https://doi.org/10.1039/c6sc00595k.
[60] E.C. Constable, P. Harverson, J.J. Ramsden, Adsorption of ruthenadendrimers to silica-titania surfaces studied by optical waveguide lightmode spectroscopy (OWLS), Chem. Commun. (1997) 1683–1684, https://doi.org/10.1039/a704638c.
[61] E. Balaur, C. Sadatnajafi, B. Abbey, Optical barcoding using polarisation sensitive plasmonic biosensors for the detection of self-assembled monolayers, Sci. Rep. 12 (2022) 1–10, https://doi.org/10.1038/s41598-022-16804-0.
[62] D. Blasi, L. Sarcina, A. Tricase, A. Stefanachi, F. Leonetti, D. Alberga, G. F. Mangiatordi, K. Manoli, G. Scamarcio, R.A. Picca, L. Torsi, Enhancing the sensitivity of biotinylated surfaces by tailoring the design of the mixed self-assembled monolayer synthesis, ACS Omega. 5 (2020) 16762–16771, https://doi.org/10.1021/acsomega.0c01717.
[63] T. Sun, Y. Zhang, F. Zhao, N. Xia, L. Liu, Self-assembled biotin-phenylalanine nanoparticles for the signal amplification of surface plasmon resonance biosensors, Microchim. Acta. 187 (2020), https://doi.org/10.1007/s00604-020-04461-x.
[64] A. Fernández, J.J. Ramsden, On adsorption-induced denaturation of folded proteins, J. Biol. Phys. Chem. 1 (2001) 81–84, https://doi.org/10.4024/12fe011l.01.02.
[65] E. Farkas, R. Tarr, A. Saftics, D. Kinga, B. Stercz, J. Domokos, B. Peter, S. Kurunczi, I. Szekacs, A. Bony, B. Anita, P. Fürjes, S. Ruszkai-szaniszl, E. Ostorh, Development and in-depth characterization of bacteria repellent and bacteria adhesive antibody-coated surfaces using optical waveguide biosensing, Biosensors. 12 (2022) 1–20, https://doi.org/10.3390/bios12020056.
[66] N. Kovacs, D. Patko, N. Orgovan, S. Kurunczi, J.J. Ramsden, F. Vonderviszt, R. Horvath, Optical anisotropy of flagellin layers: In situ and label-free measurement of adsorbed protein orientation using OWLS, Anal. Chem. 85 (2013) 5382–5389, https://doi.org/10.1021/ac3034322.
[67] R. Horvath, J.J. Ramsden, Quasi-isotropic analysis of anisotropic thin films on optical waveguides, Langmuir. 23 (2007) 9330–9334, https://doi.org/10.1021/la701405n.
[68] A.M. Ferrie, Q. Wu, O.D. Deichmann, Y. Fang, High frequency resonant waveguide grating imager for assessing drug-induced cardiotoxicity, Appl. Phys. Lett. 104 (2014) 1–6, https://doi.org/10.1063/1.4876095.
[69] M. Sztilkovics, T. Gerecsei, B. Peter, A. Saftics, S. Kurunczi, I. Szekacs, B. Szabo, R. Horvath, Single-cell adhesion force kinetics of cell populations from combined

label-free optical biosensor and robotic fluidic force microscopy, Sci. Rep. 10 (2020) 1–13, https://doi.org/10.1038/s41598-019-56898-7.
[70] N.K. Febles, S. Chandrasekaran, Y. Fang, Resonant waveguide grating imager for single cell monitoring of the invasion of 3D speheroid cancer cells through matrigel, Methods Mol. Biol. 1571 (2017) 143–160, https://doi.org/10.1007/978-1-4939-6848-0_10.
[71] K. Tiefenthaler, W. Lukosz, Sensitivity of grating couplers as integrated-optical chemical sensors, J. Opt. Soc. Am. B. 6 (1989) 209–220, https://doi.org/10.1364/josab.6.000209.
[72] J.A. De Feijter, J. Benjamins, F.A. Veer, Ellipsometry as a tool to study the adsorption behavior of synthetic and biopolymers at the air–water interface, Biopolymers. 17 (1978) 1759–1772, https://doi.org/10.1002/bip.1978.360170711.
[73] N. Orgovan, D. Patko, C. Hos, S. Kurunczi, B. Szabó, J.J. Ramsden, R. Horvath, Sample handling in surface sensitive chemical and biological sensing: A practical review of basic fluidics and analyte transport, Adv. Colloid Interf. Sci. 211 (2014) 1–16, https://doi.org/10.1016/j.cis.2014.03.011.
[74] Q. Sun, N. Zhang, Z. Li, Y. Wang, Nanoparticle-stabilized foam for effective displacement in porous media and enhanced oil recovery, Energy Technol. 4 (2016) 1053–1063, https://doi.org/10.1002/ente.201600063.
[75] A.R.B.G. Halsey, Adsorption of Long-chain aliphatic amines on glass vessels, Nat. Int. J. Sci. 196 (1962) 1048–1050.
[76] J. McColl, R. Horvath, G.E. Yakubov, J.J. Ramsden, Surface rearrangement of adsorbed EGCG–mucin complexes on hydrophilic surfaces, Int. J. Biol. Macromol. 95 (2017) 704–712, https://doi.org/10.1016/j.ijbiomac.2016.11.108.
[77] P.G. De Gennes, The dynamics of reactive wetting on solid surfaces, Physica A. (1998) 196–205, https://doi.org/10.1016/S0378-4371(97)00466-4.
[78] R. Konradi, M. Textor, E. Reimhult, Using complementary acoustic and optical techniques for quantitative monitoring of biomolecular adsorption at interfaces, Biosensors. 2 (2012) 341–376, https://doi.org/10.3390/bios2040341.
[79] A. West, Experimental Methods to Investigate Self-Assembly at Interfaces, 21 (2017) 131-241. doi: 10.1016/B978-0-12-801970-2.00003-3.
[80] X.H. Zhang, Quartz crystal microbalance study of the interfacial nanobubbles, Phys. Chem. Chem. Phys. 10 (2008) 6842–6848, https://doi.org/10.1039/b810587a.
[81] N.F. Bonet, D.G. Cava, M. Vélez, Quartz crystal microbalance and atomic force microscopy to characterize mimetic systems based on supported lipids bilayer, Front. Mol. Biosci. 9 (2022) 1–17, https://doi.org/10.3389/fmolb.2022.935376.
[82] D. Johannsmann, A. Langhoff, C. Leppin, Studying soft interfaces with shear waves: Principles and applications of the quartz crystal microbalance (qcm), Sensors. 21 (2021), https://doi.org/10.3390/s21103490.
[83] F.A. Banville, T. Söllradl, P.-J. Zermatten, M. Grandbois, P.G. Charette, Improved resolution in SPR and MCWG microscopy by combining images acquired with distinct mode propagation directions, Opt. Lett. 40 (2015) 1165, https://doi.org/10.1364/ol.40.001165.
[84] J. Hu, X. Huang, S. Xue, G. Yesilbas, A. Knoll, O. Schneider, Measurement of the mass sensitivity of QCM with ring electrodes using electrodeposition, Electrochem. Commun. 116 (2020) 106744, https://doi.org/10.1016/j.elecom.2020.106744.
[85] L. Rodríguez-Pardo, J.F. Rodríguez, C. Gabrielli, H. Perrot, R. Brendel, Sensitivity, noise, and Resolution in QCM sensors in liquid media, IEEE Sens. J. 5 (2005) 1251–1256, https://doi.org/10.1109/JSEN.2005.859257.
[86] I. Székács, N. Kaszás, P. Gróf, K. Erdélyi, I. Szendro, B. Mihalik, Á. Pataki, F. A. Antoni, E. Madarász, Optical waveguide lightmode spectroscopic techniques for investigating membrane-bound ion channel activities, PLoS One. 8 (2013), https://doi.org/10.1371/journal.pone.0081398.
[87] E.M. Yeatman, Resolution and sensitivity in surface plasmon microscopy and sensing, Biosens. Bioelectron. 11 (1996) 635–649, https://doi.org/10.1016/0956-5663(96)83298-2.
[88] Q. Zhan, J.R. Leger, High-resolution imaging ellipsometer, Appl. Opt. 41 (2002) 4443, https://doi.org/10.1364/ao.41.004443.
[89] L. Wang, C. Zhao, M.H.G. Duits, F. Mugele, I. Siretanu, Detection of ion adsorption at solid-liquid interfaces using internal reflection ellipsometry, Sensors Actuat. B-Chem. 210 (2015) 649–655, https://doi.org/10.1016/j.snb.2014.12.127.
[90] B. Kalas, E. Agocs, A. Romanenko, P. Petrik, In situ characterization of biomaterials at solid-liquid interfaces using ellipsometry in the UV-Visible-NIR wavelength range, Phys. Status Solidi A. 216 (2019) 1–9, https://doi.org/10.1002/pssa.201800762.
[91] G. Steiner, Surface plasmon resonance imaging, Anal. Bioanal. Chem. 379 (2004) 328–331, https://doi.org/10.1007/s00216-004-2636-8.
[92] J.M. Brockman, B.P. Nelson, R.M. Corn, SPR imaging measurements of ultrathin organic films, Ann. Rev. Phys. Chem. 51 (2000) 41–63.
[93] L.S. Jung, C.T. Campbell, T.M. Chinowsky, M.N. Mar, S.S. Yee, Quantitative interpretation of the response of surface plasmon resonance sensors to adsorbed films, Langmuir. 14 (1998) 5636–5648, https://doi.org/10.1021/la971228b.
[94] E. Bužavaitė-Vertelienė, V. Maciulis, J. Anulytė, T. Tolenis, A. Baskys, I. Plikusiene, Z. Balevičius, Total internal reflection ellipsometry approach for bloch surface waves biosensing applications, Biosensors. 12 (2022) 4–13, https://doi.org/10.3390/bios12080584.
[95] A.M. Ferrie, Q. Wu, Y. Fang, Resonant waveguide grating imager for live cell sensing, Appl. Phys. Lett. 97 (2010), https://doi.org/10.1063/1.3522894.
[96] R. Ungai-Salánki, E. Haty, T. Gerecsei, B. Francz, B. Béres, M. Sztilkovics, I. Székács, B. Szabó, R. Horvath, Single-cell adhesion strength and contact density drops in the M phase of cancer cells, Sci. Rep. 11 (2021) 1–13, https://doi.org/10.1038/s41598-021-97734-1.
[97] H. Wu, J. Luo, X. Huang, L. Wang, Z. Guo, J. Liang, S. Zhang, H. Xue, J. Gao, Superhydrophobic, mechanically durable coatings for controllable light and magnetism driven actuators, J. Colloid Interf. Sci. 603 (2021) 282–290, https://doi.org/10.1016/j.jcis.2021.06.106.
[98] L. Zheng, S. Handschuh-Wang, Z. Ye, B. Wang, Liquid metal droplets enabled soft robots, Appl. Mater. Today. 27 (2022) 101423, https://doi.org/10.1016/j.apmt.2022.101423.
[99] B. Wang, S. Handschuh-Wang, J. Shen, X. Zhou, Z. Guo, W. Liu, M. Pumera, L. Zhang, Small-scale robotics with tailored wettability, Adv. Mater. 35 (2023) 1–28, https://doi.org/10.1002/adma.202205732.
[100] Y. Chen, Y. Zhang, H. Li, J. Shen, F. Zhang, J. He, J. Lin, B. Wang, S. Niu, Z. Han, Z. Guo, Bioinspired hydrogel actuator for soft robotics: opportunity and challenges, Nano Today. 49 (2023) 101764, https://doi.org/10.1016/j.nantod.2023.101764.
[101] B. Kwak, S. Choi, J. Maeng, J. Bae, Marangoni effect inspired robotic self-propulsion over a water surface using a flow-imbibition-powered microfluidic pump, Sci. Rep. 11 (2021) 1–13, https://doi.org/10.1038/s41598-021-96553-8.
[102] S.I. Pearlman, E.M. Tang, Y.K. Tao, F.R. Haselton, Controlling droplet marangoni flows to improve microscopy-based TB diagnosis, Diagnostics. 11 (2021), https://doi.org/10.3390/diagnostics11112155.
[103] J. Shen, X. Zhang, H. Zhong, W. Cheng, Y. Li, Particle concentration distribution control based on shear rate gradient and marangoni convection in microchannel, IOP Conf. Ser. Mater. Sci. Eng. 538 (2019), https://doi.org/10.1088/1757-899X/538/1/012057.
[104] M. Park, S.L. Tsai, W. Chen, Microbial biosensors: Engineered microorganisms as the sensing machinery, Sensors. 13 (2013) 5777–5795, https://doi.org/10.3390/s130505777.
[105] N. Rezaee, J. Aunna, J. Naser, Investigation of recirculating marangoni flow in three-dimensional geometry of aqueous micro-foams, Fluids. 8 (2023), https://doi.org/10.3390/fluids8040113.